crystals

MDPI

Article

Characterization, Concentration, and Speciation of Metal Elements in Copper Slag: Implications for Secondary Metal Recovery

Zirou Liu [1], Xinhang Xu [1], Li Guo [1], Qiusong Chen [1] and Chongchong Qi [1,2,*]

[1] School of Resources and Safety Engineering, Central South University, Changsha 410083, China; liuziroustudy@gmail.com (Z.L.); x578817460@163.com (X.X.); llguo98@163.com (L.G.); qiusong.chen@csu.edu.cn (Q.C.)
[2] School of Metallurgy and Environment, Central South University, Changsha 410083, China
* Correspondence: chongchong.qi@csu.edu.cn

Abstract: The treatment of large amounts of copper slag is an unavoidable issue resulting from the high demand for copper during the global transition to a sustainable development path. Metal-rich copper slag might serve as a potential source of metals through secondary recovery. In this study, two copper slags (CS1 and CS2) with different metallurgical properties were characterized, focusing on secondary metal recovery. The X-ray diffraction (XRD) results show that fayalite (Fe_2SiO_4) and magnetite (Fe_3O_4) were the main crystalline phases in both CS1 and CS2. In addition, CS2 exhibited a more stable amorphous silicate network than CS1, which was attributed to the differences in the content of Si-O-3NBO linkages. The sequential extraction of Zn, Cu, Fe, and Pb from the slags was also explored, with the Cu content in CS1 being substantially lower than that in CS2. All metals were distributed in the F5 residue fraction. Cu was the most mobile metal as a result of the large proportion of soluble fractions (F1–F3), followed by Zn and Fe. This study explored the chemical speciation of Zn, Cu, Fe, and Pb from copper slags, which has practical implications for secondary metal recovery from such materials.

Keywords: copper slag; metal elements; BCR extraction method; metal recovery

Citation: Liu, Z.; Xu, X.; Guo, L.; Chen, Q.; Qi, C. Characterization, Concentration, and Speciation of Metal Elements in Copper Slag: Implications for Secondary Metal Recovery. *Crystals* **2024**, *14*, 420. https://doi.org/10.3390/cryst14050420

Academic Editor: Shouxun Ji

Received: 29 March 2024
Revised: 23 April 2024
Accepted: 26 April 2024
Published: 29 April 2024

1. Introduction

Climate change and energy consumption are driving the world towards a sustainable development path [1–3], and over the next 30–50 years, a stable supply of copper will be an essential factor in this process [4,5]. The global demand for copper is expected to reach approximately 62 million tons by 2050, with a substantial increase in this demand coming from renewable energy plants and electric vehicles [6,7]. Meeting such a large demand for copper presents both technical and environmental challenges [8,9].

Copper slag is a byproduct of the copper extraction process, and the vast majority of copper slag is discarded and disposed of as waste [10,11]. For every ton of copper produced, approximately 2.2–3 tons of copper slag are generated [12,13]. With a guaranteed demand for copper, global copper slag production is expected to increase considerably and exceed 136.4 million tons by 2050 [14,15], leading to environmental problems, such as an increasing need for landfill space. Therefore, addressing the issues arising from meeting the demand for copper is a critical step toward sustainable development.

Solid waste utilization is an approach to achieving sustainable development in many fields [16]. The construction industry has been considered a promising market for copper slag recycling [17]. For example, Mohamad et al. [18] showed that replacing 40% of fine sand with copper slag was effective in increasing the compressive and bending strength of concrete by 30% and 14%, respectively. In another study, Rajasekar et al. [19] produced ultra-high-strength concrete by replacing quartz sand with copper slag, leading to superior

durability properties. Furthermore, Gursel et al. [20] showed that an increased copper slag substitution rate lowered the energy consumption and environmental impact of concrete. However, researchers have also observed that an excessively high copper slag content would introduce new problems, such as concrete bleeding and a decrease in compressive strength [21,22]. Moreover, metals in the copper slag might leach out of the concrete, posing a serious environmental threat [23].

The recovery of metals from copper slag, known as secondary metal recovery, not only maximizes the value of resources, but also responds to stable market demand [24]. Nowadays, secondary metal recovery is an important research direction for copper slag utilization and recycling and has received increased attention in recent years [25,26]. For example, Shi et al. [27] studied the effect of calcium borate additives on copper precipitation from copper slag. Furthermore, Roy et al. [28] investigated the recovery of copper from smelting slag by ammonia and sulfuric acid leaching and demonstrated that sulfuric acid is more favorable as a leaching agent at atmospheric pressure. To date, researchers have mainly employed cumbersome leaching processes to assess secondary metal recovery from copper slag. Moreover, the underlying mechanism behind the recovery differences among copper slag samples remains poorly understood.

Therefore, in this study, we systematically characterized two copper slag samples by analyzing their physical, chemical, and surface properties and the differences in their silicate networks. In addition, we investigated the distribution patterns of Zn, Cu, Fe, and Pb in the copper slag samples and determined the feasibility of their recovery. This study has important practical implications for treating large amounts of copper slag, a new source of valuable metals.

2. Experimental Methods

2.1. Copper Slag Sampling and Preparation

The copper slag samples were obtained from two mining and metallurgy companies. Copper slag 1 (CS1) was sampled from Anqing Jin'an Mining Industry Co., Ltd., located in the Qingtian Township Government Institute, Yuexi County, Anqing, Anhui Province, China (32°25′19″ N, 115°58′45″ E). The slag was obtained via the Ausmelt technology, which is a complex pyrometallurgical process for extracting metals from metal minerals and wastes [29]. The raw materials were crushed and pre-treated, then introduced into the Ausmelt furnace for smelting. Oxygen was added to maintain proper redox condition, ensuring the accuracy and stability of the smelting reaction. The metal would be separated from the raw materials for collection, while the slag was byproduct generated during the smelting process [30,31]. Copper slag 2 (CS2) was sampled from Jinlong Copper Co., Ltd., located in Gongshan Town, Nanling County, Wuhu, Anhui Province, China (30°55′44″ N, 117°47′33″ E). The slag was obtained via the (Outotec) Double flash technology, which was a high-temperature redox smelting process for treating metal sulfide minerals [32,33]. The raw materials were crushed and pre-treated, then introduced into the Double flash furnace. During the flash smelting, the sulfur along with some non-ferrous substances in the minerals were oxidized to form metallic substances. In the converter, metallic substances were further extracted and refined to collect the metal, with the slag being a byproduct of the smelting process [34,35]. Both the slag samples were treated by slow cooling in a ladle (24 h of free air cooling and 48 h of cooling under water sprays) [36]. The samples were obtained from the cleaned slags following milling and flotation, after which they were air-dried and stored for subsequent investigations [37].

2.2. Characterization Experiments

The true density of the copper slag samples was measured using a TD-1100 true density analyzer (Beijing Builder Electronic Technology Co., Ltd., Beijing, China), and their pH was determined with an 848 Titrino plus automatic potentiometric titrator (Swiss Aptar China Ltd., Suzhou, China) at a solid–water ratio of 1:1 [38]. The samples were immersed in deionized water at a 1:1 solid–water ratio and the electrical conductivity

(EC) was measured using a Raycom DDSJ-308F conductivity meter (Shanghai Oustor™ Industrial Co., Shanghai, China) [38]. The cation exchange capacity (CEC) was measured via the hexamminecobalt (III) trichloride solution-spectrophotometric method [39,40], and the elemental composition was determined using an S4 Pioneer X-ray fluorescence (XRF) spectrometer (Bruker AXS, Karlsruhe, Germany). The particle size distributions and specific surface areas were obtained using a Mastersizer 3000 particle size analyzer (Malvern Panalytical, Malvern, UK) according to the manufacturer's instructions [41]. Surface images were obtained by scanning electron microscopy (SEM; JEOL IT-500HR, Tokyo, Japan).

The phase composition of the copper slag was analyzed by X-ray diffraction [42,43] (XRD; Empyrean, PANalytical, Almelo, The Netherlands). The samples were loaded directly onto the quartz substrate, and the XRD patterns were fitted using the Rietveld method and GSAS 1.00 software [44,45]. The original XRD profile and the ZnO structure file were simultaneously loaded into the TOPAS quantitative analysis software [46], and parameters such as the goniometer radius of the equipment and the zero-correction value were set. The cell parameters, atomic coordinates, scattering factors, and fitting were modified after the corresponding phase structure files were imported. The relative fraction of each crystal phase was obtained using TOPAS. The amorphous phase fraction can only be calculated using the crystal phase fraction; therefore, 20% ZnO was added before the XRD experiments to carry out the normalization process.

The Fourier transform infrared (FTIR) spectra of the copper slags were recorded using a Nicolet iS50 FTIR spectrometer (Thermo Fisher Scientific, Waltham, MA, USA) in the wave number range of 4000–400 cm^{-1}. The samples and KBr powder were compacted together and loaded onto the sample plate. The FTIR spectra were deconvoluted in the wave number range of 1150–750 cm^{-1}. Because of the overlapping absorption peaks present in this region, deconvolution (a half peak width of 40 cm^{-1} and a band enhancement factor of 3) was performed using the OMNIC software, and the second-order derivatives of the spectra were obtained using the 7-point Savitzky–Golay function. The relative positions of the overlapping peaks were obtained by referring to the deconvolution and second-order derivatives of the infrared spectra in this region. The Origin software was used for baseline selection, and the residuals were minimized by multiple Gaussian curve fitting to calculate the area of each sub-peak.

Depth profiling was performed on Thermo Scientific™ K-Alpha™ (Thermo Scientific, Waltham, MA, USA). The etching time was selected as 0 s, 100 s, 200 s, and 300 s. The monochromated Al target (E = 1486.68 eV) was selected as the excitation source type with an etch voltage of 3000 eV. The pass energies of 150 eV and 30–40 eV were chosen for the full and fine spectra, respectively. The vacuum was less than 1.0×10^{-8} mbar with the work function of 4.2 eV. The binding energies (BEs) of the spectra were all calibrated with the hydrocarbon contamination C 1s peak located at 284.8 eV because no organic matter was present. When fitting the spectra with the XPS Peak 4.1 software, a Shirley background was selected. The overlapping of the peaks due to core-level splitting was fixed and a Gaussian/Lorentzian hybrid function was used to describe the peak patterns. Gaussian peak fitting is a common data-fitting method to fit data with multiple peaks [47] and extract useful information [48]. This method involves superimposing multiple Gaussian functions to generate a compound function and then fitting the data using the least squares method.

2.3. Pseudo-Total Concentrations

Pseudo-total concentrations were determined by microwave-assisted digestion (30 min, 180 °C, 1200 W, and 10 bar) of the copper slag samples (~0.5 g) with concentrated HF, HNO_3, and $HClO_4$ in Teflon® PFA containers. Thereafter, the samples were placed on a hot plate and evaporated to dryness. The elemental concentrations of the solutions were measured using an inductively coupled plasma-optical emission spectrometer (ICP-OES) (Thermo Electro Co., Waltham, MA, USA). Pseudo-total concentrations were obtained because the acid digestion might not have completely destroyed the silicates, leaving a small amount of metal within the copper slags.

2.4. Sequential Extraction Experiments

The sequential extraction method, used to analyze chemical forms [49], was performed in this study following the Commission of the European Communities (BCR) extraction procedure [50,51], with modifications. The process was carried out as described below.

For the water-soluble fraction (F1), 1 g of the CS1 and CS2 samples was placed into corresponding 50 mL polypropylene bottles, 40 mL of ultrapure water was added, and the mixture was shaken at 25 °C for 16 h. For the acid-soluble fraction (F2), 40 mL of 0.11 mol·L^{-1} CH_3COOH was added to the residue of F1 and was shaken at 25 °C for 16 h. To obtain the reducible fraction (F3), 40 mL of 0.5 mol·L^{-1} $NH_2OH{\cdot}HCl$ (pH = 1.5, adjusted with HNO_3) was added to the residue of F2 and shaken at 25 °C for 16 h. For the oxidizable fraction (F4), 10 mL of 30% H_2O_2 was added to the residue of F3; the mixture was shaken at 25 °C for 1 h, and the liquid was then evaporated by shaking at 85 °C for 1 h. Subsequently, another 10 mL of 30% H_2O_2 was added and evaporated by shaking at 85 °C for 1 h. Next, 50 mL of 1.0 mol·L^{-1} CH_3COONH_4 (pH = 2, adjusted with HNO_3) was added, and the mixture was shaken at 25 °C for 16 h. The final residue fraction (F5) was obtained by adding 2.5 mL of 46% HF, 7 mL of 60% HNO_3, and 0.5 mL of 30% H_2O_2 to the F4 residue in a Teflon container, which was microwaved at 220 °C for 20 min.

The copper slag samples were passed through a 0.15 mm sieve before conducting the sequential extraction experiments [52]. After centrifugation at 3000 rpm for 20 min, the supernatant from each step was separated from the solid residue and decanted into a polyethylene tube. The fine particles were removed from the supernatant using a 0.20 µm membrane filter. The solid residue from each step was washed by adding 20 mL of deionized water and shaking the mixture for 15 min; after centrifugal separation and discarding the supernatant, the residue was used in the subsequent steps. Moreover, the leaching percentage was defined as the ratio of the leached amount to the total elemental content, that is, the sum of the elemental contents of F1 to F5 [53].

3. Results and Discussion

3.1. Basic Characterization of Copper Slag Samples

Tables 1 and 2 present the physical and chemical properties of the CS1 and CS2 samples, respectively; differences are observed between CS1 and CS2 as they were produced via different processes. Differences in the contents of different chemical components such as S, Cu, Ca, and Mg between the CS1 and CS2 significantly affected their pH and CEC values. CS1 has a lower pH because of its high S content, while its lower Cu, Ca, and Mg contents may be contributing to its higher CEC values. These differences may be attributed to two different production processes (Ausmelt and Double flash technologies) that affect the distribution of chemical constituents and thus the physical and chemical properties.

Table 1. Physical properties of copper slag samples.

Parameters	CS1	CS2	Parameters	CS1	CS2
True Density (g/cm^3)	3.98	3.91	Electrical conductivity (mS/cm)	24.30	23.30
pH	6.85	7.08	CEC (cmol$^+$/kg)	61.40	59.50

Table 2. Chemical composition of copper slag samples.

Component	CS1 (wt.%)	CS2 (wt.%)	Component	CS1 (wt.%)	CS2 (wt.%)
O	38.90	38.50	Mo	0.13	0.30
Fe	34.95	34.31	Ba	0.11	0.02
Si	16.40	15.84	As	0.09	0.17
Al	3.01	2.59	Mn	0.05	0.05
Zn	1.42	1.34	P	0.04	0.04
K	1.20	1.02	Cr	0.03	0.01
Ca	1.15	2.66	Sb	0.02	0.02

Table 2. *Cont.*

Component	CS1 (wt.%)	CS2 (wt.%)	Component	CS1 (wt.%)	CS2 (wt.%)
Mg	0.85	1.36	Cl	0.01	0.01
Na	0.72	0.86	Ni	0.01	n.d.
Pb	0.24	0.25	Sr	0.01	0.01
S	0.20	0.08	V	0.01	0.01
Ti	0.18	0.16	Co	n.d.	0.01
Cu	0.14	0.29			

Figure 1 shows the cumulative particle size distribution of the copper slag samples. The accumulation percentages of CS1 and CS2 exceed 88% at 66.89 and 100 µm, respectively, and CS1 exhibits a smaller particle size distribution and larger specific surface area than CS2. CS1 has a smaller particle size distribution and a larger specific surface area which lead to more surface contact as well as a tighter packing, thus contributing to the physical properties of higher conductivity and true density of CS1 than CS2.

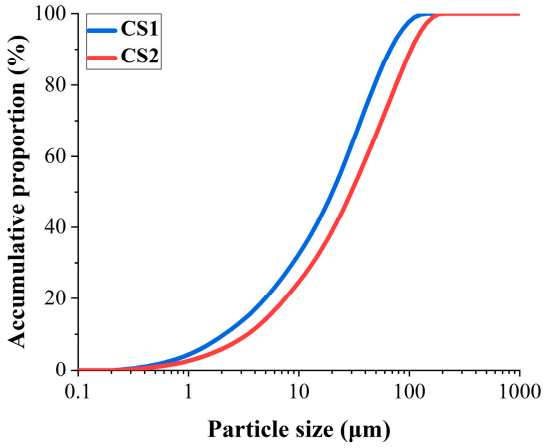

Figure 1. Particle size accumulation distribution of copper slag samples.

Figure 2 depicts the SEM images of CS1 and CS2 at different magnifications. The slags consist of irregular particles with sharp edges and a glassy appearance on their surfaces, indicating the presence of glass phases.

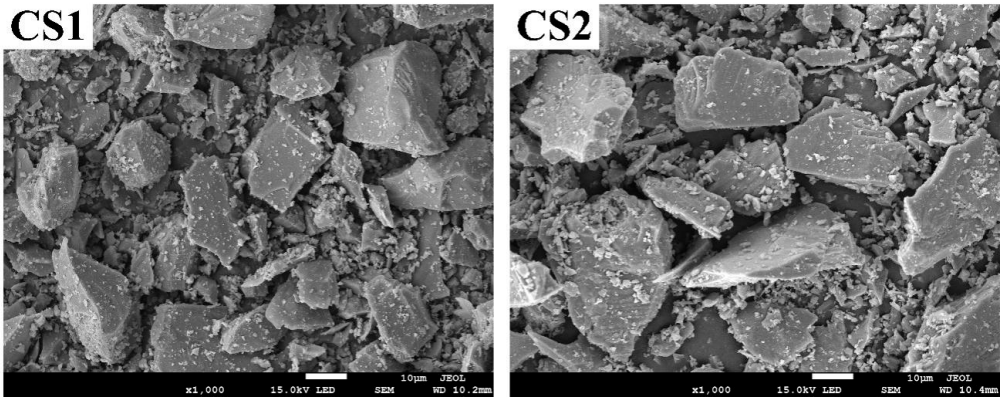

Figure 2. SEM image of the copper slag samples. The magnification was ×1000.

3.2. XRD Analysis

Figure 3 shows the XRD spectra of the copper slag samples. CS1 and CS2 exhibit the same percentage composition of amorphous phases (37.37%), and their major crystalline phases include fayalite (Fe_2SiO_4) and magnetite (Fe_3O_4), in agreement with the litera-

ture [54,55]. The proportion of fayalite in CS1 is 8.38% higher than that in CS2, indicating a notable difference in their compositions.

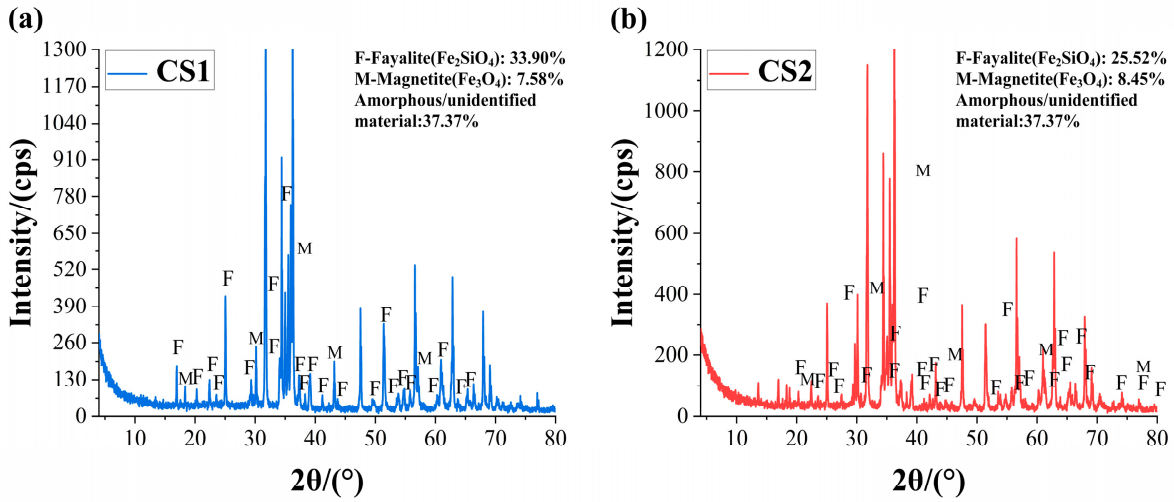

Figure 3. The XRD patterns of the copper slag samples. (**a**) CS1 and (**b**) CS2. The percentages of substance compositions are noted inside the figure.

3.3. FTIR Spectral Analysis

Figure 4 presents the FTIR spectra of the copper slag samples, which show two main transmittance bands associated with the characteristic vibrations of silicates. The first occurs between 400 and 600 cm^{-1} and is associated with Si-O-Si bending vibrations [56,57], and the second appears between 700 and 1200 cm^{-1} and is associated with the stretching vibrations of the SiO_4 tetrahedral groups [58,59]. The peak near 827 cm^{-1} is attributed to Si-O-Si symmetric stretching [27], and those near 873, 921, 948, and 2049 cm^{-1} are assigned to the stretching vibrations of Si-O-4NBO, Si-O-3NBO, Si-O-2NBO, and Si-O-1NBO, respectively [60,61]. The second major transmittance band is analyzed using Gaussian peak fitting to investigate the differences in the connection structures of the silicates in CS1 and CS2, as shown in Figure 5 [62].

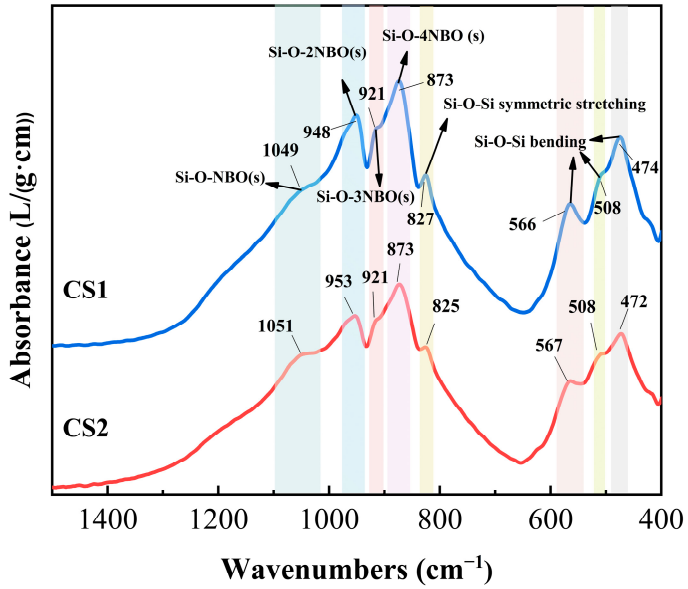

Figure 4. FTIR spectra of CS1 (marked in **blue**) and CS2 (marked in **red**). The corresponding functional group positions are noted inside the figure.

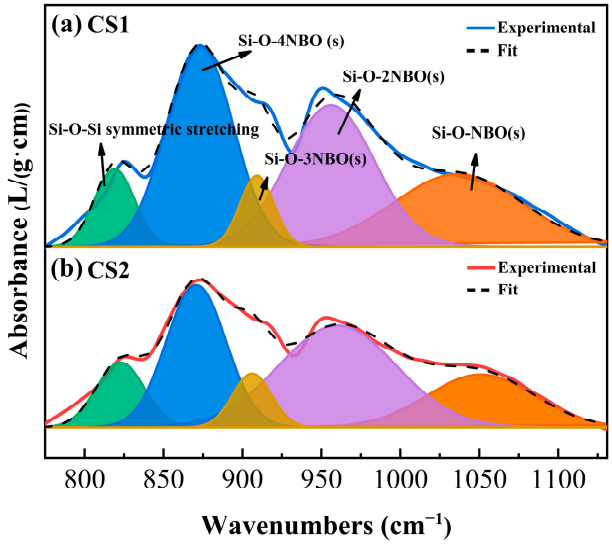

Figure 5. Deconvolution FTIR spectra of (**a**) CS1 and (**b**) CS2 in the range of 775–1130 cm^{-1}.

Figure 5 displays the deconvoluted FTIR spectra of CS1 and CS2. The deconvoluted peaks are assigned to five major vibrations, which are consistent with the results in Figure 4. Table 3 shows the characteristic peak parameters of the CS samples. The peak near 826 cm^{-1} is related to Si-O-Si symmetric stretching [27], and the relative areas of this vibration for CS1 and CS2 are 7.69% and 27.12%, respectively. Moreover, the relative areas of the Si-O-4NBO, Si-O-2NBO, and Si-O-1NBO peaks exhibit no substantial differences between the samples. Finally, the relative areas of Si-O-3NBO for CS1 and CS2 are 30.37% and 9.98%, respectively. The above results indicate that CS2 has a stronger covalent Si-O-Si bonds connecting the SiO_4 tetrahedra and fewer NBO ionic bonds than CS1, implying that CS2 exhibits a more stable amorphous silicate network [62].

Table 3. Deconvolution characteristic peak parameters of copper slag samples.

Assignments	CS1		CS2	
	Fitting Center (cm^{-1})	Relative Area (%)	Fitting Center (cm^{-1})	Relative Area (%)
Si-O-Si symmetric stretching	827	7.69	825	27.12
Si-O-4NBO	873	33.07	873	38.21
Si-O-3NBO	921	30.37	921	9.98
Si-O-2NBO	948	5.91	953	6.65
Si-O-1NBO	1049	22.96	1051	18.04

3.4. XPS Analysis

Figure 6 shows the XPS spectra of the CS samples at the etching time of 300 s, where the main characteristic peak is that of O1s [23]. The Zn 2p, Cu 2p, Fe 2p, and Pb 4f peaks are observed in both samples, which is consistent with the analysis in Table 2. The spectra of Zn 2p, Cu 2p, Fe 2p, and Pb 4f are shown in Figure 7 for a further analysis of the surface chemical composition of the four elements [63,64].

The deconvoluted XPS spectrum at the etching times of 0 s, 100 s, and 200 s are provided in the Supplementary Materials (Figures S1–S3). Figure 7 shows the deconvoluted XPS spectra of the copper slag samples at the etching time of 300 s; the predominant peaks of CS1 at 1044.7 and 1021.7 eV (ΔBE = 23 eV) in Figure 7a are attributed to the Zn $2p_{1/2}$ and Zn $2p_{3/2}$ signals of ZnO, respectively [65,66]. In the Zn 2p region of CS2 in Figure 7a, Zn 2p signals with substantially decreased intensity are also detected at 1044.6 and 1021.6 eV, indicating the presence of ZnO in CS2. As shown in Figure 7b, the fine scan spectra of Cu 2p could be fitted by the peaks located at 934.0 and 954.0 eV, corresponding to Cu $2p_{3/2}$ and Cu $2p_{1/2}$, respectively, where the spin-orbit splitting energy is determined to be 19.75 eV [67].

The peaks at 934.0 and 954.0 eV are considered to be Cu^{2+}, which was also observed in the sequential extraction experiments [68–71]. In Figure 7c, the BE peaks of 724.2, 723.0, 720.3, 713.6, 710.0, and 706.0 eV are attributed to Fe_2O_3 $2p_{1/2}$, Fe^{2+} $2p_{1/2}$, Fe $2p_{1/2}$, Fe_2O_3 $2p_{3/2}$, Fe^{2+} $2p_{3/2}$, and Fe $2p_{3/2}$, respectively [72,73]. The signal for the Fe arises from the reduction of iron oxide by Al ions during deep etching. In Figure 7d, the BE peaks of 144.7 and 139.8 eV are attributed to the Pb $4f_{5/2}$ and Pb $4f_{7/2}$ signals of Pb_3O_4, respectively, with a ΔBE of 4.9 eV [74]. The observed differences in Pb, as compared to the PbO forms observed in the literature [75], can be attributed to factors including surface oxidation, peak overlap, and the XPS predominantly characterizing the surface composition.

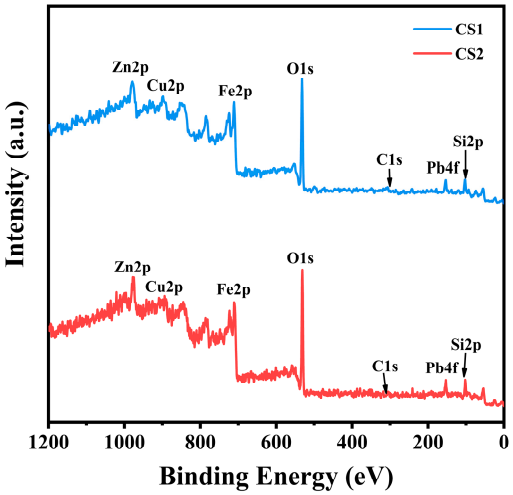

Figure 6. XPS survey spectra of copper slag samples.

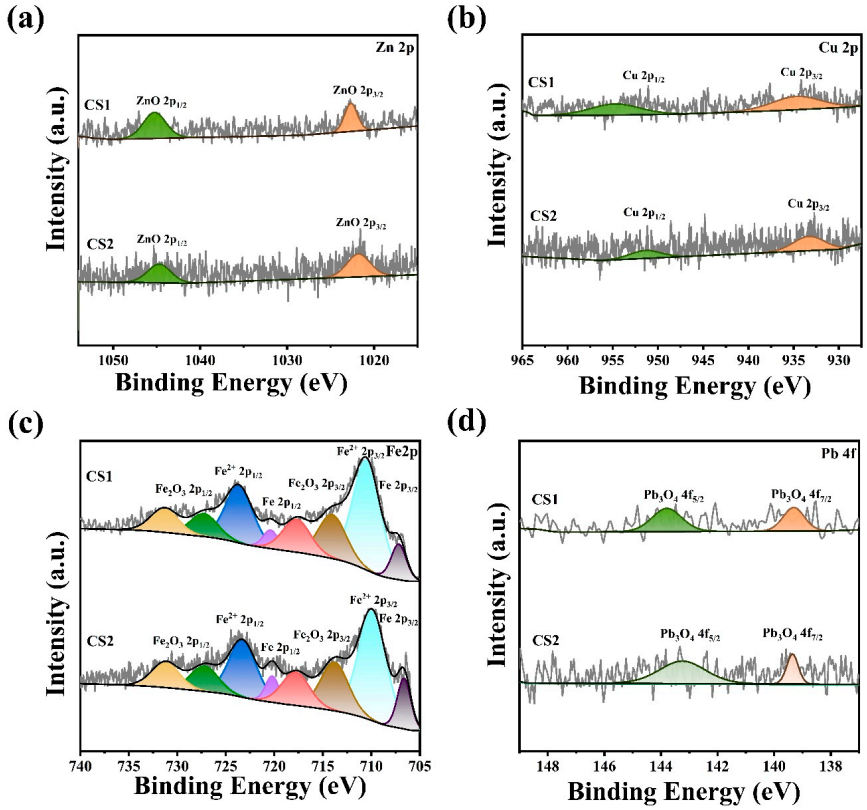

Figure 7. Fine scan XPS spectra of the copper slag samples at the etching time of 300 s: (**a**) Zn 2p, (**b**) Cu 2p, (**c**) Fe 2p, and (**d**) Pb 4f. The gray line shows the experimental values. The black line shows the fitted values of CS1 and CS2.

3.5. Sequential Extraction Analysis

Figure 8 shows the results of the sequential extraction of Zn, Cu, Fe, and Pb from CS1 and CS2, and Tables 4 and 5 present the numerical results. The total Zn content in CS1 and CS2 is 18,589.3 and 16,613.0 mg/kg, respectively. Moreover, the sum of the leaching percentages of F1 to F4 is 24.8% for CS1 and 19.1% for CS2, suggesting a higher susceptibility of Zn to leaching in CS1. In F1, the leaching percentage of Zn is 0.26% for CS1 and 0.02% for CS2, indicating that Zn is more easily released in the former than in the latter in an ultrapure water environment. This effect may be related to the higher Zn content on the surface of CS1 relative to CS2, as shown in the XPS analysis. In F2 and F3, the slags leach more Zn than in F1, which is significantly attributed to the solubilization of ZnO [76,77]. The XRD data demonstrate the presence of Zn-containing minerals, while the XPS analysis confirms the presence of Zn primarily in the form of ZnO on the slag surface. The higher leaching in CS1 could be a result of the greater surface exposure of ZnO, as suggested by the intensity of the Zn peaks in the XPS spectra. In F4, CS1 leached more Zn than CS2 due to the higher ZnS content of CS1 than CS2, as shown in Table 2 [78,79]. Moreover, more than 75% of the Zn in CS1 and CS2 is leached in F5, which is associated with Zn's integration into the silicate matrix, a conclusion supported by the FTIR analysis that shows a strong Si-O network where Zn could be complexed.

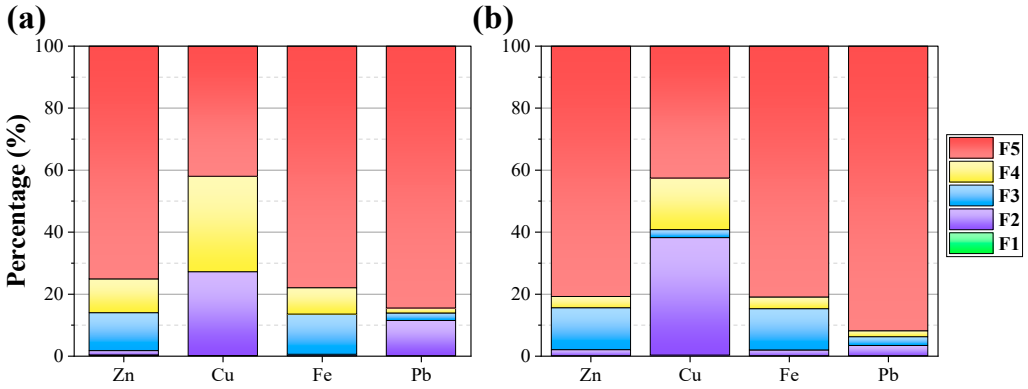

Figure 8. The sequential extraction results of the Zn, Cu, Fe, and Pb elements from the copper slag samples: (**a**) CS1 and (**b**) CS2.

The total Cu content of CS2 is twice that of CS1, which is consistent with the results in Table 2. In F1, the leaching content of CS1 and CS2 is very low: 1.6 and 8.8 mg/kg, respectively. By contrast, in F2, the samples exhibit high leaching contents of 500 and 1458 mg/kg, respectively, which may be attributed to the contribution of acid-soluble CuO [80,81]. This heightened leaching can be largely ascribed to the dissolution of acid-soluble CuO, a supposition supported by the XPS data which identified copper predominantly in the Cu^{2+} state. In F2, CS1 and CS2 exhibit 27.09% and 37.96% leaching, respectively, demonstrating the high bioavailability and instability of Cu [82]. In F3, CS2 yields 97.1 mg/kg, while no effective leaching is observed for CS1. In F4, the samples exhibit similar leached Cu contents, related to the sulfide fraction and organocopper compounds, detailed by the fine scan XPS spectra [83–85]. The F5 fraction of Cu in CS1 and CS2 is approximately 42%, the smallest among the four elements. This implies that a significant portion of copper remains bound within the silicate matrix, and is only released upon the application of the rigorous extraction conditions inherent to F5. The congruence of the leaching rates in this fraction further underscores the XRD findings of a substantial and stable silicate network within the slags.

Table 4. The sequential extraction results of the Zn, Cu, Fe, and Pb elements from the CS1 sample.

Elements (mg/kg)	Zn	Cu	Fe	Pb
F1	47.5	1.6	4.6	0.2
Leaching degree (%)	0.26	0.09	0.00	0.01
F2	262.5	500.0	1756.6	293.5
Leaching degree (%)	1.41	27.09	0.48	11.37
F3	2281.8	0.0	47,780.0	62.9
Leaching degree (%)	12.27	0.00	12.96	2.44
F4	2018.7	567.5	31,562.5	41.4
Leaching degree (%)	10.86	30.75	8.56	1.60
F5	13,978.7	776.3	287,577.5	2182.3
Leaching degree (%)	75.20	42.07	78.00	84.58
Total element content	18,589.2	1845.4	368,681.2	2580.3
Pseudo-total concentrations	15,619.3	1518.9	243,351.2	1862.1

Table 5. The sequential extraction results of the Zn, Cu, Fe, and Pb elements from the CS2 sample.

Elements (mg/kg)	Zn	Cu	Fe	Pb
F1	2.8	8.8	5.8	0.2
Leaching degree (%)	0.02	0.23	0.00	0.01
F2	328.3	1458.0	6554.0	83.6
Leaching degree (%)	1.98	37.96	1.89	3.31
F3	2243.8	97.1	46,300.0	72.0
Leaching degree (%)	13.51	2.53	13.32	2.85
F4	606.5	641.0	13,135.0	48.3
Leaching degree (%)	3.65	16.69	3.78	1.91
F5	13,431.5	1636.4	281,518.0	2320.8
Leaching degree (%)	80.85	42.60	81.01	91.92
Total element content	16,612.9	3841.3	347,512.8	2524.9
Pseudo-total concentrations	12,005.5	2861.5	298,735.8	2217.6

The leaching percentages of Fe in CS1 and CS2 are similar to those of Zn. Tables 4 and 5 show that most of the Fe is residual in F5. The leached content of Fe in F3 is greater than in the other fractions, which is mainly attributed to the oxide contribution of Fe–Mn, with XRD identifying iron-rich phases and XPS confirming the presence of both Fe^{2+} and Fe^{3+} [86,87]. Moreover, CS1 shows a greater leaching content than CS2 in F4. The specific XRD data, which shows a greater presence of fayalite in CS1, combined with the FTIR spectra indicating more non-bridging oxygen environments within its silicate matrix, suggests a more complex and less stable iron structure. The XPS analysis corroborates this by revealing a higher ratio of Fe^{2+} and Fe^{3+} on the surface of CS1 compared to CS2, which could facilitate the oxidation and subsequent leaching of iron in the F4 fraction. The Pb content in F5 is 84.57% and 91.91% for CS1 and CS2, respectively, indicating that Pb exists mainly in the silicate form and is difficult to leach from the copper slags. Furthermore, the XPS analysis provides evidence of oxidized Pb species, such as Pb_3O_4, on the slag surface, which might contribute to its persistence in the matrix until the highly aggressive conditions of F5.

More than 75% of the Zn, Fe, and Pb contents are present in notably stable phases in CS1 and CS2, and the percentage of Pb in CS2 reaches 91.92%. Because of the high total content of Fe and Zn in the copper slags, even at lower leaching rates, more of these metals may be extracted than other metals with lower concentrations but higher leaching rates.

Approximately 42% Cu is present in F5 of CS1 and CS2, the leaching of which is difficult [88]. Approximately 27% and 37% Cu could be easily leached in the natural environments represented by CS1 and CS2, respectively. Moreover, these results show that the proportion of elemental residues in CS2 is higher than in CS1, as confirmed by the FTIR analysis, because of the more stable amorphous silicate network of CS2 compared to CS1.

3.6. Significance of the Study

This work characterized two copper slags and investigated their metal element distribution using sequential extraction methods. The results revealed that Zn and Fe in the copper slags can exhibit very high leaching contents, even at low leaching rates, because of the high original contents of both metals. Elemental Cu can be leached at a high rate in the natural environment, and Pb mainly exists in a stable phase in the copper slags. These observations indicate that the two copper slags display great potential for Zn, Cu, and Fe extraction. Furthermore, our results have practical implications for treating large amounts of copper slag. For example, the characterization results show that most of the Pb in the copper slag exists in the form of stabilized silicates. This is essential for environmental safety because it means that even if these copper slags are used in landfills or as building materials, only a small fraction of the Pb in the slag will be released, which helps us to better assess and manage the environmental risks when planning the disposal strategy for the copper slags. Finally, secondary metal recovery from copper slag is consistent with the concept of circular economy and sustainable development [89], and this study provides a theoretical basis for the recovery of Cu, Zn, and Fe metals from copper slag.

4. Conclusions

Copper slags from two processes were analyzed and characterized via XRD, FTIR, and XPS. The leaching behavior of selected metals in the copper slags was investigated using sequential extraction. The main findings of the study are as follows:

1. The physical and chemical properties of the CS1 and CS2 samples were different; for example, CS1 had a lower pH than CS2, and the elemental Cu content of CS1 was less than half that of CS2.
2. The XRD results revealed that CS1 and CS2 had the same percentage composition of amorphous phases (37.37%), and their major crystalline phases were fayalite (Fe_2SiO_4) and magnetite (Fe_3O_4).
3. The FTIR spectra revealed that CS2 had a more stable amorphous silicate network than CS1.
4. The sequential extraction results show that, because of the high Fe and Zn contents of the copper slags, high leaching contents can be obtained, even at low leaching percentages. This indicates that copper slags are effective sources of Fe and Zn extraction, which is one of the significant values for secondary recovery. In the natural environment, approximately 27% and 37% of Cu could be easily leached from CS1 and CS2, respectively. Elemental Pb in the samples existed mainly as a stable phase. Furthermore, the above results clarified the distribution and existence forms of the four elements in copper slags, which provided a theoretical basis for the design of a more effective secondary recovery process.

Supplementary Materials: The following supporting information can be downloaded at: https://www.mdpi.com/article/10.3390/cryst14050420/s1, Figure S1: Fine scan XPS spectra of the copper slag samples at the etching time of 0 s: (**a**) Zn 2p, (**b**) Cu 2p, (**c**) Fe 2p, and (**d**) Pb 4f. The gray line shows the experimental values. The black line shows the fitted values of CS1 and CS2; Figure S2: Fine scan XPS spectra of the copper slag samples at the etching time of 100 s: (**a**) Zn 2p, (**b**) Cu 2p, (**c**) Fe 2p, and (**d**) Pb 4f. The gray line shows the experimental values. The black line shows the fitted values of CS1 and CS2; Figure S3: Fine scan XPS spectra of the copper slag samples at the etching time of 200 s: (**a**) Zn 2p, (**b**) Cu 2p, (**c**) Fe 2p, and (**d**) Pb 4f. The gray line shows the experimental values. The black line shows the fitted values of CS1 and CS2.

Author Contributions: Conceptualization, Z.L., X.X. and C.Q.; methodology, Z.L., X.X. and C.Q.; writing—original draft, Z.L., X.X. and C.Q.; writing—review and editing, Z.L., X.X., L.G., Q.C. and C.Q.; supervision, C.Q.; funding acquisition, Q.C. and C.Q. All authors have read and agreed to the published version of the manuscript.

Funding: This work was supported by the National Natural Science Foundation of China, grant number 52004330.

Data Availability Statement: The raw data supporting the conclusions of this article will be made available by the authors upon request.

Conflicts of Interest: The authors declare no conflicts of interest.

References

1. Colasante, A.; D'Adamo, I.; Morone, P. What drives the solar energy transition? The effect of policies, incentives and behavior in a cross-country comparison. *Energy Res. Soc. Sci.* **2022**, *85*, 102405. [CrossRef]
2. Rivera, N.; Guzmán, J.I.; Jara, J.J.; Lagos, G. Evaluation of econometric models of secondary refined copper supply. *Resour. Policy* **2021**, *73*, 102170. [CrossRef]
3. Xu, X.; Qi, C.; Aretxabaleta, X.M.; Ma, C.; Spagnoli, D.; Manzano, H. The initial stages of cement hydration at the molecular level. *Nat. Commun.* **2024**, *15*, 2731. [CrossRef]
4. Hund, K.; La Porta, D.; Fabregas, T.P.; Laing, T.; Drexhage, J. *Minerals for Climate Action: The Mineral Intensity of the Clean Energy Transition*; World Bank: Singapore, 2020.
5. Harmsen, J.H.M.; Roes, A.L.; Patel, M.K. The impact of copper scarcity on the efficiency of 2050 global renewable energy scenarios. *Energy* **2013**, *50*, 62–73. [CrossRef]
6. Watari, T.; Northey, S.; Giurco, D.; Hata, S.; Yokoi, R.; Nansai, K.; Nakajima, K. Global copper cycles and greenhouse gas emissions in a 1.5 °C world. *Resour. Conserv. Recycl.* **2022**, *179*, 106118. [CrossRef]
7. Zhang, L.; Chen, Z.; Yang, C.; Xu, Z. Global supply risk assessment of the metals used in clean energy technologies. *J. Clean. Prod.* **2022**, *331*, 129602. [CrossRef]
8. Fuentes, M.; Negrete, M.; Herrera-León, S.; Kraslawski, A. Classification of indicators measuring environmental sustainability of mining and processing of copper. *Miner. Eng.* **2021**, *170*, 107033. [CrossRef]
9. Phiri, T.C.; Singh, P.; Nikoloski, A.N. The potential for copper slag waste as a resource for a circular economy: A review—Part II. *Miner. Eng.* **2021**, *172*, 107150. [CrossRef]
10. Sharifi, Y.; Afshoon, I.; Asad-Abadi, S.; Aslani, F. Environmental protection by using waste copper slag as a coarse aggregate in self-compacting concrete. *J. Environ. Manag.* **2020**, *271*, 111013. [CrossRef] [PubMed]
11. Wang, M.; Yu, W.; Zeng, D.; Zhu, L.; Gao, C.; Hu, M.; Le, C.; Qiu, T. Volatilization of Zn and Pb and preparation of integrated micro-electrolysis filter from copper slag and its application for removing Cr(VI) from aqueous solution. *Chemosphere* **2022**, *288*, 132596. [CrossRef]
12. Kumar, A.; Tejaswini, M.L. Studies on hardened properties of concrete incorporated with copper slag. *Mater. Today Proc.* **2022**, *60*, 646–657. [CrossRef]
13. Mikula, K.; Skrzypczak, D.; Izydorczyk, G.; Baśladyńska, S.; Szustakiewicz, K.; Gorazda, K.; Moustakas, K.; Chojnacka, K.; Witek-Krowiak, A. From hazardous waste to fertilizer: Recovery of high-value metals from smelter slags. *Chemosphere* **2022**, *297*, 134226. [CrossRef] [PubMed]
14. Holland, K.; Eriç, R.H.; Taskinen, P.; Jokilaakso, A. Upgrading copper slag cleaning tailings for re-use. *Miner. Eng.* **2019**, *133*, 35–42. [CrossRef]
15. Filipović, S.; Đokić, O.; Radević, A.; Zakić, D. Copper Slag of Pyroxene Composition as a Partial Replacement of Natural Aggregate for Concrete Production. *Minerals* **2021**, *11*, 439. [CrossRef]
16. Murari, K.; Siddique, R.; Jain, K.K. Use of waste copper slag, a sustainable material. *J. Mater. Cycles Waste Manag.* **2015**, *17*, 13–26. [CrossRef]
17. Wang, R.; Shi, Q.; Li, Y.; Cao, Z.; Si, Z. A critical review on the use of copper slag (CS) as a substitute constituent in concrete. *Constr. Build. Mater.* **2021**, *292*, 123371. [CrossRef]
18. Peirovi, M.; Labafzadeh, M.S.; Dehghani, A.; Meftahi, F. Durability and mechanical properties of precast concrete curb containing waste copper slag. *Mag. Concr. Res.* **2019**, *71*, 567–576. [CrossRef]
19. Rajasekar, A.; Arunachalam, K.; Kottaisamy, M. Assessment of strength and durability characteristics of copper slag incorporated ultra high strength concrete. *J. Clean. Prod.* **2019**, *208*, 402–414. [CrossRef]
20. Gursel, A.P.; Ostertag, C. Life-Cycle Assessment of High-Strength Concrete Mixtures with Copper Slag as Sand Replacement. *Adv. Civ. Eng.* **2019**, *2019*, 6815348. [CrossRef]
21. Al-Jabri, K.S.; Hisada, M.; Al-Oraimi, S.K.; Al-Saidy, A.H. Copper slag as sand replacement for high performance concrete. *Cem. Concr. Compos.* **2009**, *31*, 483–488.
22. Al-Jabri, K.S.; Al-Saidy, A.H.; Taha, R. Effect of copper slag as a fine aggregate on the properties of cement mortars and concrete. *Constr. Build. Mater.* **2011**, *25*, 933–938. [CrossRef]
23. He, R.; Zhang, S.; Zhang, X.; Zhang, Z.; Zhao, Y.; Ding, H. Copper slag: The leaching behavior of heavy metals and its applicability as a supplementary cementitious material. *J. Environ. Chem. Eng.* **2021**, *9*, 105132. [CrossRef]
24. Phiri, T.C.; Singh, P.; Nikoloski, A.N. The potential for copper slag waste as a resource for a circular economy: A review—Part I. *Miner. Eng.* **2022**, *180*, 107474. [CrossRef]

25. Linsong, W.; Zhiyong, G.; Honghu, T.; Li, W.; Haisheng, H.; Wei, S.; Yongbao, Q.; Yue, Y. Copper recovery from copper slags through flotation enhanced by sodium carbonate synergistic mechanical activation. *J. Environ. Chem. Eng.* **2022**, *10*, 107671. [CrossRef]
26. Zheng, W.; He, D.; Wang, Y.; Chen, J.; Xue, M.; Li, H. Preparation of cement-based color facing mortar by copper pyrometallurgical slag modification: Efficient utilization of high-iron-content slag. *J. Environ. Chem. Eng.* **2021**, *9*, 105888. [CrossRef]
27. Shi, Y.; Li, B.; Dai, G.; Zhou, S.; Wang, H.; Wei, Y. Effect of calcium borate on sedimentation of copper inclusions in copper slag. *Chin. J. Process Eng.* **2019**, *19*, 553–559.
28. Roy, S.; Sarkar, S.; Datta, A.; Rehani, S. Importance of mineralogy and reaction kinetics for selecting leaching methods of copper from copper smelter slag. *Sep. Sci. Technol.* **2016**, *51*, 135–146. [CrossRef]
29. Hughes, S.; Reuter, M.A.; Baxter, R.; Kaye, A.; Hughes, S.; Reuter, M.; Baxter, R.; Kaye, A. Ausmelt technology for lead and zinc processing. *Lead Zinc* **2008**, *2008*, 147–162.
30. Mounsey, E.N.; Robilliard, K.R. Sulfide smelting using ausmelt technology. *JOM* **1994**, *46*, 58–60. [CrossRef]
31. Hughes, S.; Reuter, M.; Kaye, A. *Ausmelt Technology-Developments in Copper*; Metalexpo Annual Exhibition: Moscow, Russia, October 2007.
32. Kaur, R.; Nexhip, C.; Krippner, D.; George-Kennedy, D.; Routledge, M. Kennecott-Outotec 'double flash'technology after 16 years. In Proceedings of the 13th International Flash Smelting Congress, Livingstone, Zambia, 1 October 2011.
33. Han, F.; Yu, F.; Cui, Z. Industrial metabolism of copper and sulfur in a copper-specific eco-industrial park in China. *J. Clean. Prod.* **2016**, *133*, 459–466. [CrossRef]
34. Mackey, P. Evolution of the Large Copper Smelter—1800s to 2013. In *Celebrating the Megascale: Proceedings of the Extraction and Processing Division Symposium on Pyrometallurgy in Honor of David GC Robertson*; Springer: Berlin/Heidelberg, Germany, 2016; pp. 17–37.
35. Kojo, I.; Lahtinen, M.; Miettinen, E. Flash converting–sustainable technology now and in the future. In *International Peirce-Smith Converting Centennial*; Outotec Oyj: Espoo, Finland, 2009.
36. Mihajlović, A.; Kamberović, Ž.; Korać, M.; Gavrilovski, M.; Jovanović, N. The effect of cooling rate of slag from primary copper production in the valorization of copper in the flotation process. *Metall. Mater. Eng.* **2015**, *21*, 127–141. [CrossRef] [PubMed]
37. Wang, J.-X.; Xu, D.-M.; Fu, R.-B.; Chen, J.-P. Bioavailability Assessment of Heavy Metals Using Various Multi-Element Extractants in an Indigenous Zinc Smelting Contaminated Site, Southwestern China. *Int. J. Environ. Res. Public Health* **2021**, *18*, 8560. [CrossRef] [PubMed]
38. Lim, T.-T.; Chu, J. Assessment of the use of spent copper slag for land reclamation. *Waste Manag. Res.* **2006**, *24*, 67–73. [CrossRef] [PubMed]
39. Ma, Y.; Cheng, L.; Zhang, D.; Zhang, F.; Zhou, S.; Ma, Y.; Guo, J.; Zhang, Y.; Xing, B. Stabilization of Pb, Cd, and Zn in soil by modified-zeolite: Mechanisms and evaluation of effectiveness. *Sci. Total Environ.* **2022**, *814*, 152746. [CrossRef] [PubMed]
40. Dong, M.; Huang, R.; Mao, P.; Lei, L.; Li, Y.; Li, Y.; Xia, H.; Li, Z.; Zhuang, P. Immobilization of Cadmium by Molecular Sieve and Wollastonite Is Soil pH and Organic Matter Dependent. *Int. J. Environ. Res. Public Health* **2021**, *18*, 5128. [CrossRef] [PubMed]
41. Mastersizer 3000 Manual. Available online: https://www.manualslib.com/manual/1524845/Malvern-Mastersizer-3000.html#manual (accessed on 9 September 2021).
42. Yang, J.; Jeon, D.; Kang, H.; Shang, X.; Moon, J. Hydrophobic treatment on hollow glass microspheres for enhancing the flowability of lightweight high-performance cementitious composites. *Constr. Build. Mater.* **2023**, *409*, 133856. [CrossRef]
43. Yang, J.; Kang, H.; Shi, C.; Hu, X.; Moon, J. Tomographic analysis of segregation behavior of hollow glass microspheres in lightweight cementitious composites. *Cem. Concr. Compos.* **2024**, *149*, 105516. [CrossRef]
44. Zhao, P.; Liu, X.; De La Torre, A.; Lu, L.; Sobolev, K. Assessment of the quantitative accuracy of Rietveld/XRD analysis of crystalline and amorphous phases in fly ash. *Anal. Methods* **2017**, *9*, 2415–2424. [CrossRef]
45. Larson, A.C.; Von Dreele, R.B. Gsas. *Rep. Laur* **1994**, 86–748.
46. Liu, H.; Zhao, P.; Wang, S.; Gong, C.; Lu, L. Rietveld Quantitative Analysis of Amorphous Phase in Slag by Internal Standard Method. In Proceedings of the 2018 10th International Conference on Measuring Technology and Mechatronics Automation (ICMTMA), Changsha, China, 10–11 February 2018; pp. 379–382.
47. Swann, G.E.A.; Patwardhan, S.V. Application of Fourier Transform Infrared Spectroscopy (FTIR) for assessing biogenic silica sample purity in geochemical analyses and palaeoenvironmental research. *Clim. Past* **2011**, *7*, 65–74. [CrossRef]
48. Abdel-Aal, R.E. Comparison of Algorithmic and Machine Learning Approaches for the Automatic Fitting of Gaussian Peaks. *Neural Comput. Appl.* **2002**, *11*, 17–29. [CrossRef]
49. Qi, C.; Wu, M.; Liu, H.; Liang, Y.; Liu, X.; Lin, Z. Machine learning exploration of the mobility and environmental assessment of toxic elements in mining-associated solid wastes. *J. Clean. Prod.* **2023**, *401*, 136771. [CrossRef]
50. Tian, Q.; Guo, B.; Nakama, S.; Sasaki, K. Distributions and Leaching Behaviors of Toxic Elements in Fly Ash. *ACS Omega* **2018**, *3*, 13055–13064. [CrossRef] [PubMed]
51. Zhang, Y.; Shang, P.; Wang, J.; Norris, P.; Romero, C.E.; Pan, W.-P. Trace element (Hg, As, Cr, Cd, Pb) distribution and speciation in coal-fired power plants. *Fuel* **2017**, *208*, 647–654. [CrossRef]
52. Li, J.; Kosugi, T.; Riya, S.; Hashimoto, Y.; Hou, H.; Terada, A.; Hosomi, M. Pollution potential leaching index as a tool to assess water leaching risk of arsenic in excavated urban soils. *Ecotoxicol. Environ. Saf.* **2018**, *147*, 72–79. [CrossRef]

53. Van Herck, P.; Vandecasteele, C. Evaluation of the use of a sequential extraction procedure for the characterization and treatment of metal containing solid waste. *Waste Manag.* **2001**, *21*, 685–694. [CrossRef] [PubMed]
54. Li, K.-Q.; Ping, S.; Wang, H.-Y.; Ni, W. Recovery of iron from copper slag by deep reduction and magnetic beneficiation. *Int. J. Miner. Metall. Mater.* **2013**, *20*, 1035–1041. [CrossRef]
55. Gabasiane, T.S.; Danha, G.; Mamvura, T.A.; Mashifana, T.; Dzinomwa, G. Characterization of copper slag for beneficiation of iron and copper. *Heliyon* **2021**, *7*, e06757. [CrossRef] [PubMed]
56. Aguiar, H.; Serra, J.; González, P.; León, B. Structural study of sol–gel silicate glasses by IR and Raman spectroscopies. *J. Non-Cryst. Solids* **2009**, *355*, 475–480. [CrossRef]
57. Rada, S.; Dehelean, A.; Stan, M.; Chelcea, R.; Culea, E. Structural studies on iron–tellurite glasses prepared by sol–gel method. *J. Alloys Compd.* **2011**, *509*, 147–151. [CrossRef]
58. Meng, X.; Li, Y.; Wang, H.; Yang, Y.; McLean, A. Effects of Na_2O additions to copper slag on iron recovery and the generation of ceramics from the non-magnetic residue. *J. Hazard. Mater.* **2020**, *399*, 122845. [CrossRef] [PubMed]
59. Zhao, Z.W.; Chai, L.Y.; Peng, B.; Liang, Y.J.; He, Y.; Yan, Z.H. Arsenic vitrification by copper slag based glass: Mechanism and stability studies. *J. Non-Cryst. Solids* **2017**, *466–467*, 21–28. [CrossRef]
60. Park, H.; Park, J.Y.; Kim, G.H.; Sohn, I. Effect of TiO_2 on the viscosity and slag structure in blast furnace type slags. *Steel Res. Int.* **2012**, *83*, 150–156. [CrossRef]
61. Zhang, Z.; Xie, B.; Zhou, W.; Diao, J.; Li, H.-Y. Structural characterization of $FeO–SiO_2–V_2O_3$ slags using molecular dynamics simulations and FT-IR spectroscopy. *ISIJ Int.* **2016**, *56*, 828–834. [CrossRef]
62. Feng, Y.; Chen, Q.; Zhou, Y.; Yang, Q.; Zhang, Q.; Jiang, L.; Guo, H. Modification of glass structure via CaO addition in granulated copper slag to enhance its pozzolanic activity. *Constr. Build. Mater.* **2020**, *240*, 117970. [CrossRef]
63. Korin, E.; Froumin, N.; Cohen, S. Surface Analysis of Nanocomplexes by X-ray Photoelectron Spectroscopy (XPS). *ACS Biomater. Sci. Eng.* **2017**, *3*, 882–889. [CrossRef] [PubMed]
64. Ku, J.; Zhang, L.; Fu, W.; Wang, S.; Yin, W.; Chen, H. Mechanistic study on calcium ion diffusion into fayalite: A step toward sustainable management of copper slag. *J. Hazard. Mater.* **2021**, *410*, 124630. [CrossRef] [PubMed]
65. Park, D.; Tak, Y.; Kim, J.; Yong, K. Low-temperature synthesized ZnO nanoneedles: XPS and PL analysis. *Surf. Rev. Lett.* **2007**, *14*, 1061–1065. [CrossRef]
66. Iaiche, S.; Djelloul, A. $ZnO/ZnAl_2O_4$ nanocomposite films studied by X-ray diffraction, FTIR, and X-ray photoelectron spectroscopy. *J. Spectrosc.* **2015**, *2015*, 836859. [CrossRef]
67. Poulston, S.; Parlett, P.; Stone, P.; Bowker, M. Surface oxidation and reduction of CuO and Cu_2O studied using XPS and XAES. *Surf. Interface Anal.* **1996**, *24*, 811–820. [CrossRef]
68. Tian, X.; Li, X.; Bi, P. Effect of O-isobutyl-N-ethyl thionocarbamates on flotation behavior of porphyry copper ore and its adsorption mechanism. *Appl. Surf. Sci.* **2020**, *503*, 144313. [CrossRef]
69. Biesinger, M.C. Advanced analysis of copper X-ray photoelectron spectra. *Surf. Interface Anal.* **2017**, *49*, 1325–1334. [CrossRef]
70. Van der Heide, P. *X-ray Photoelectron Spectroscopy: An Introduction to Principles and Practices*; John Wiley & Sons: Hoboken, NJ, USA, 2011.
71. Gorai, B.; Jana, R. Characteristics and utilisation of copper slag—A review. *Resour. Conserv. Recycl.* **2003**, *39*, 299–313. [CrossRef]
72. Carraro, G.; Gasparotto, A.; Maccato, C.; Peeters, D.; Barreca, D. Fe_2O_3-CuO nanocomposites prepared by a two-step vapor phase strategy and analyzed by XPS. *Surf. Sci. Spectra* **2014**, *21*, 1–9. [CrossRef] [PubMed]
73. Yamashita, T.; Hayes, P. Analysis of XPS spectra of Fe^{2+} and Fe^{3+} ions in oxide materials. *Appl. Surf. Sci.* **2008**, *254*, 2441–2449. [CrossRef]
74. Thomas, J.M.; Tricker, M.J. Electronic structure of the oxides of lead. Part 2.—An XPS study of bulk rhombic PbO, tetragonal PbO, β-PbO_2 and Pb_3O_4. *J. Chem. Soc. Faraday Trans. 2* **1975**, *71*, 329–336. [CrossRef]
75. Sineva, S.; Shevchenko, M.; Shishin, D.; Hidayat, T.; Chen, J.; Hayes, P.C.; Jak, E. Phase Equilibria and Minor Element Distributions in Complex Copper/Slag/Matte Systems. *JOM* **2020**, *72*, 3401–3409. [CrossRef]
76. Rüşen, A.; Topçu, M.A. Investigation of zinc extraction from different leach residues by acid leaching. *Int. J. Environ. Sci. Technol.* **2018**, *15*, 69–80. [CrossRef]
77. Wang, X.; Zhong, Y.; Kang, Y.; Gao, J.; Guo, Z. Promoted Acid Leaching of Zn from Hazardous Zinc-Containing Metallurgical Dusts: Focusing on Transformation of Zn Phases in Selective Reduction Roasting. *Process Saf. Environ. Prot.* **2022**, *163*, 353–361. [CrossRef]
78. Ettler, V.; Mihaljevič, M.; Šebek, O.; Molek, M.; Grygar, T.; Zeman, J. Geochemical and Pb isotopic evidence for sources and dispersal of metal contamination in stream sediments from the mining and smelting district of Příbram, Czech Republic. *Environ. Pollut.* **2006**, *142*, 409–417. [CrossRef] [PubMed]
79. Tian, H.; Guo, Z.; Pan, J.; Zhu, D.; Yang, C.; Xue, Y.; Li, S.; Wang, D. Comprehensive review on metallurgical recycling and cleaning of copper slag. *Resour. Conserv. Recycl.* **2021**, *168*, 105366. [CrossRef]
80. Zhang, M.; Guo, X.; Tian, B.; Wang, J.; Qi, S.; Yang, Y.; Xin, B. Improved bioleaching of copper and zinc from brake pad waste by low-temperature thermal pretreatment and its mechanisms. *Waste Manag.* **2019**, *87*, 629–635. [CrossRef] [PubMed]
81. Vakylabad, A.B.; Schaffie, M.; Ranjbar, M.; Manafi, Z.; Darezereshki, E. Bio-processing of copper from combined smelter dust and flotation concentrate: A comparative study on the stirred tank and airlift reactors. *J. Hazard. Mater.* **2012**, *241*, 197–206. [CrossRef] [PubMed]

82. Chlopecka, A. Assessment of form of Cd, Zn and Pb in contaminated calcareous and gleyed soils in Southwest Poland. *Sci. Total Environ.* **1996**, *188*, 253–262. [CrossRef]
83. Rodríguez, L.; Ruiz, E.; Alonso-Azcárate, J.; Rincón, J. Heavy metal distribution and chemical speciation in tailings and soils around a Pb–Zn mine in Spain. *J. Environ. Manag.* **2009**, *90*, 1106–1116. [CrossRef] [PubMed]
84. Zhou, H.; Liu, G.; Zhang, L.; Zhou, C. Mineralogical and morphological factors affecting the separation of copper and arsenic in flash copper smelting slag flotation beneficiation process. *J. Hazard. Mater.* **2021**, *401*, 123293. [CrossRef]
85. Dung, T.T.T.; Cappuyns, V.; Swennen, R.; Vassilieva, E.; Phung, N.K. Leachability of arsenic and heavy metals from blasted copper slag and contamination of marine sediment and soil in Ninh Hoa district, south central of Vietnam. *Appl. Geochem.* **2014**, *44*, 80–92.
86. Wang, Y.; Liu, M.; Dong, N.; Lin, Y.; Chang, G.; Wei, G.; Zhao, K.; Wang, X.; Zheng, A.; Zhao, Z.; et al. Chemical looping gasification of high nitrogen wood waste using a copper slag oxygen carrier modified by alkali and alkaline earth metals. *Chem. Eng. J.* **2021**, *410*, 128344. [CrossRef]
87. Zhang, H.; Li, B.; Wei, Y.; Wang, H.; Yang, Y. Effect of CaO on Copper Loss and Phase Transformation in Copper Slag. *Metall. Mater. Trans. B* **2022**, *53*, 1538–1551. [CrossRef]
88. Pathak, A.; Rana, M.S.; Al-Sheeha, H.; Navvmani, R.; Al-Enezi, H.M.; Al-Sairafi, S.; Mishra, J. Feasibility of bioleaching integrated with a chemical oxidation process for improved leaching of valuable metals from refinery spent hydroprocessing catalyst. *Environ. Sci. Pollut. Res.* **2022**, *29*, 34288–34301. [CrossRef]
89. Gabasiane, T.S.; Danha, G.; Mamvura, T.A.; Mashifana, T.; Dzinomwa, G. Environmental and socioeconomic impact of copper slag—A review. *Crystals* **2021**, *11*, 1504. [CrossRef]